Ann. Phys. (Leipzig) **10** (2001) 11–12, 887–910

Imaging of atomic orbitals with the Atomic Force Microscope – experiments and simulations

F. J. Giessibl*, **H. Bielefeldt, S. Hembacher, and J. Mannhart**

Universität Augsburg, Institute of Physics, Electronic Correlations and Magnetism, Experimentalphysik VI, 86135 Augsburg, Germany

Received 27 June 2001, accepted 2 July 2001 by U. Eckern

Abstract. Atomic force microscopy (AFM) is a mechanical profiling technique that allows to image surfaces with atomic resolution. Recent progress in reducing the noise of this technique has led to a resolution level where previously undetectable symmetries of the images of single atoms are observed. These symmetries are related to the nature of the interatomic forces. The Si(111)-(7 × 7) surface is studied by AFM with various tips and AFM images are simulated with chemical and electrostatic model forces. The calculation of images from the tip-sample forces is explained in detail and the implications of the imaging parameters are discussed. Because the structure of the Si(111)-(7 × 7) surface is known very well, the shape of the adatom images is used to determine the tip structure. The observability of atomic orbitals by AFM and scanning tunneling microscopy is discussed.

Keywords: atomic force microscope, atomic orbitals
PACS: 68.37.Ps, 34.20.Cf, 68.35.Gy, 68.35.Ja

1 Introduction

In 1959, Schlier and Farnsworth reported their low-energy electron diffraction (LEED) experiments on the surface of Si (111) [1]. After heating the surface to 900 °C, they discovered that the surface displays additional scattering peaks in the LEED pattern. These additional peaks were caused by a reconstruction of the Si surface where the new unit cell is 7 × 7 as large as the bulk terminated structure. Silicon condenses in the diamond structure with a cubic lattice constant of $a_0 = 5.430\,\text{Å}$ at $T = 0\,\text{K}$ and $a_0 = 5.4355\,\text{Å}$ at $T = 300\,\text{K}$ [2]. The unit vectors of the bulk terminated Si (111) surface have a length of $v = a_0/\sqrt{2} = 3.84\,\text{Å}$ and an angle of 60°, in the reconstructed surface, the unit vectors have a length of $w = 7 \times 3.84\,\text{Å} = 26.88\,\text{Å}$ (see Fig. 1). The reconstruction not only affects the surface atom layer, but the topmost four layers, and the new unit cell contains approximately 200 atoms. Because of this remarkable size of the unit cell, the determination of the atom positions has been a tremendous challenge for surface scientists for more than two decades. The determination of the positions of the surface atoms by Binnig et al. with a scanning tunneling microscope (STM) in 1982 [3] was instrumental for the discovery of all the atomic positions within the surface

* franz.giessibl@physik.uni-augsburg.de

 0003-3804/01/11-1211-0887 $ 17.50+.50/0

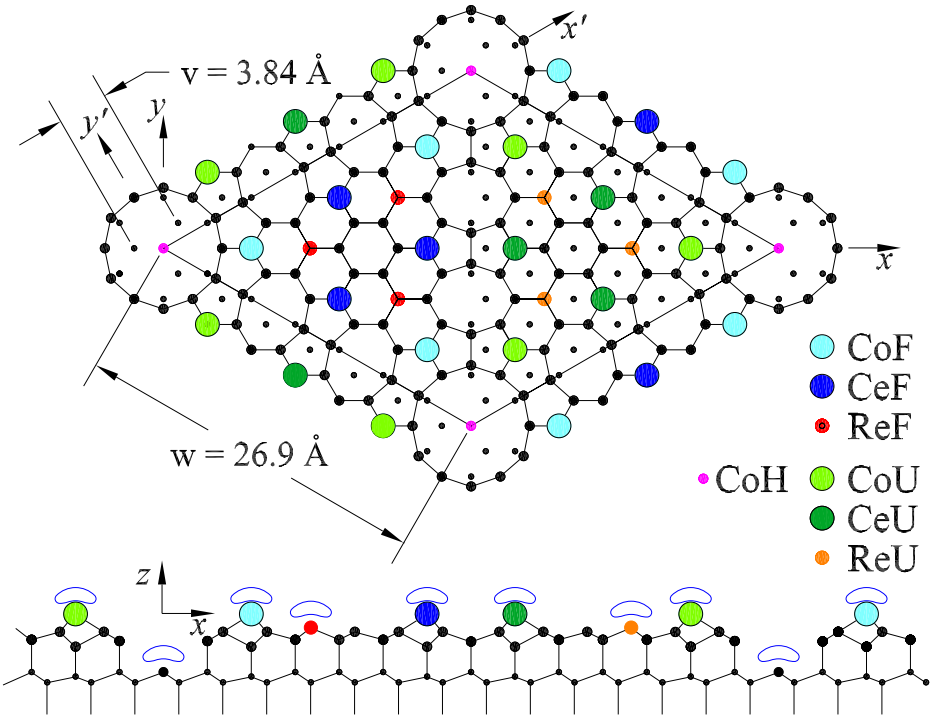

Fig. 1 Top view and cross section ($y = 0$) of the dimer-adatom-stacking fault (DAS) model of Si (111)-(7×7). The unreconstructed surface lattice has a lattice constant of 3.84 Å. By forming the 7×7 reconstruction, most of the dangling bonds of the surface atoms are saturated by an adatom such that the total number of dangling bonds per unit cell is reduced from 49 to 19. Twelve adatoms and a corner hole per unit cell are the striking features of this reconstruction. The adatoms fall into four symmetry classes: corner faulted (CoF), center faulted (CeF), corner unfaulted (CoU), center unfaulted (CeU). The 19 remaining dangling bonds originate from the 12 adatoms, the 6 rest atoms (ReF, ReU) and the atom in the center of the corner hole (CoH).

unit cell. In 1985, the now commonly adapted dimer-adatom-stacking-fault model (DAS) was finally suggested by Takayanagi et al. [4]. According to this model (see Fig. 1), six adatoms are situated in each half of the unit cell. The adatoms are bound by covalent bonds formed by sp^3 hybrid orbitals. In the bulk, the hybrid orbitals of neighboring atoms overlap and form an electron pair. At the surface, one of the four sp^3 hybrid orbitals is pointing perpendicular to the surface and forms a dangling bond.

Because of its historic role in the establishment of the STM, the Si (111)-(7 × 7) surface has been considered as a touchstone for the feasibility of the atomic force microscope (AFM) [5] as a tool for surface science. However, because of the reactivity of Si (111)-(7 × 7), AFM experiments have proven to be difficult in the quasistatic AFM mode, and chemical bonding between tip and sample has hampered atomic resolution [6]. In 1994, Si (111)-(7 × 7) was imaged by AFM for the first time [7, 8]. AFM is now becoming an increasingly powerful tool for surface science, as true atomic resolution is achieved routinely [9–11]. Surfaces are imaged with atomic re-

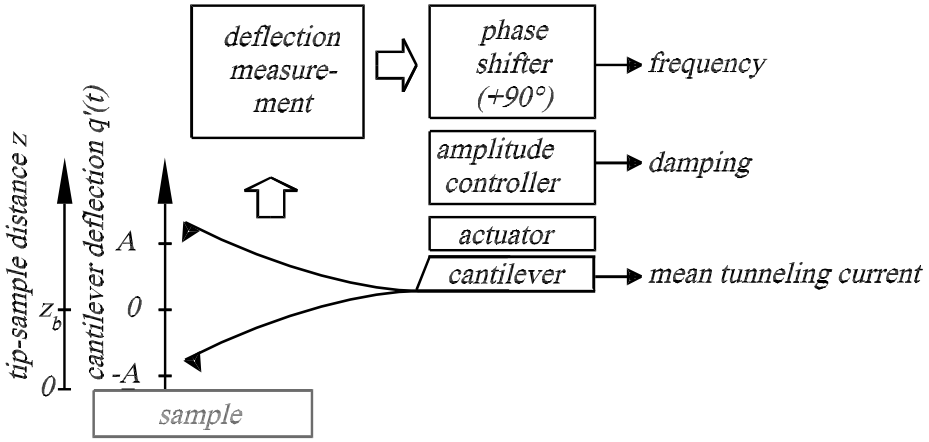

Fig. 2 Operating principle of a frequency modulation AFM. A cantilever is mounted onto an actuator, which is used to excite an oscillation at an adjustable fixed amplitude A. When forces act between tip and sample, the oscillation frequency changes. Additional observables are the driving signal which is required to operate the cantilever at a given amplitude. If sample and cantilever tip are electrically conductive, a mean tunneling current can also be measured.

solution by bringing a probe into close proximity and sensing the interaction while scanning the surface. It has been shown that a dynamic mode of imaging is required for resolving reactive surfaces like Si (111) in ultra-high vacuum where chemical bonding between tip and sample can occur [7, 8]. Frequency-Modulation AFM (FM-AFM) [12] has proven to be a practical method for fast imaging in vacuum and is now the commonly used technique. Recently, it was proposed [13] that the noise decreases by a factor of approximately 10 by optimizing the stiffness of the cantilever and the oscillation amplitude (see section 2). Consequently, unprecedented resolution has been achieved with these operating parameters. Especially, deviations from the so far hemispherical apparent shape of the individual atoms have been observed, and these deviations have been attributed to the symmetry of the chemical bonds between tip and sample.

The first AFM images of Si (111)-(7×7) [7, 8] looked similar to the STM images of the empty states. The bond between the front atom of the tip and the dangling bond on top of the adatoms is thought to be responsible for the experimentally observed atomic contrast in the FM-AFM images [14, 15]. While the atom in the center of the cornerholes is 4.45 Å below the adatoms surrounding the cornerhole [16], in typical STM experiments a depth of 2 Å is observed. The discrepancy between the nominal depth of the cornerholes and the STM data is probably caused by the finite tip radius of the STM tips. The tip is not sharp enough to allow a penetration of the front atom all the way to the bottom of the cornerhole. In the first AFM experiment, the observed depth of the cornerhole was only ≈ 0.8 Å [7]. This even smaller depth is probably due to a significant contribution of long-range forces. It is shown here, that the contribution of long-range forces is reduced by operating the microscope with very small oscillation amplitudes and a cornerhole depth of ≈ 2.5 Å is obtained.

In the present work, the Si(111)-(7×7) surface is investigated using FM-AFM with optimised resolution. The structure of the Si(111)-(7×7) surface is known very well through a large number of experimental and theoretical studies. Because of its pronounced features, such as the deep cornerholes and the widely spaced adatoms with a well defined bonding characteristic, the Si(111)-(7×7) surface is a perfect sample for studying the atomic and subatomic structure of the tip. The spatial resolution of the AFM has advanced sufficiently such that clear deviations of an *s*- or p_z-type tip have been observed [17]. Therefore, in contrast to previous studies, tip and sample switch roles now and the well defined surface is used to probe the tip, where much less information about its structure and composition is available.

2 Experimental setup

The data was taken with a modified commercial scanning tunneling microscope [18, 19] which has been outfitted with a force sensor based on a quartz tuning fork ("qPlus-sensor", [20]). The tip of the force sensor is either an etched tungsten tip such as known from STM or a silicon crystallite. In FM-AFM, a cantilever beam holding a sharp tip with an eigenfrequency f_0, spring constant k and quality factor Q is subject to controlled positive feedback such that it oscillates with a constant amplitude A. When this cantilever is brought close to a sample, its frequency changes from f_0 to $f = f_0 + \Delta f$. This frequency change Δf is used to create an image $z(x, y, \Delta f)$ by scanning the cantilever in the $x - y$ plane and recording the corresponding z-position of the base of the cantilever z_b. A feedback mechanism adjusts z_b such that Δf stays constant. In the "classic" mode of operation, typical parameters are $\Delta f \approx -100\,\mathrm{Hz}$, $k \approx 20$ N/m, $f_0 \approx 200\,\mathrm{kHz}$, $A \approx 10$ nm and $Q \approx 10^5$ – see Table 1 in Ref. [13] for an overview. Equation (1) shows that the vertical resolution in FM-AFM can be improved by reducing the amplitude A to the Å-range [13]. For tip-sample forces $F_{ts} = F_0 \exp(-z/\lambda)$ where z is the tip-sample distance, the vertical noise δz is a function of the amplitude A, the force range λ, the detection bandwidth B and the temperature T:

$$\delta z \propto \frac{\left(1 + \sqrt{\frac{\pi}{2}} \left(\frac{A}{\lambda}\right)^{3/2}\right)}{A} \sqrt{TB}\,. \tag{1}$$

Minimal noise results when $A \approx \lambda$ and for a small product of temperature and bandwidth. The bandwidth B is approximately equal to the number of pixels per second which can be recorded. Operating at a small bandwidth implies a small scanning speed and long image acquisition times, and thermal drift can become a problem. When operating at low temperatures, thermal drift is usually not present and imaging at very small scanning speeds is feasible. Operation with very small amplitudes is not possible with conventional cantilevers. In order to avoid instabilities like jump-to-contact and to minimize perturbations of the oscillation by tip-sample dissipation, it helps to use cantilevers with $k \approx 1000\,\mathrm{N/m}$ and

$Q \approx 1000$ [21]. A secondary benefit of using small amplitudes is an enhanced sensitivity to short-range forces and a reduced sensitivity to long-range forces (see Fig. 4). The oscillator electronics which controls the force sensor is designed with an emphasis on low noise such that oscillation amplitudes in the Å-range can be realized. The commercial phase-locked-loop (PLL) frequency detector is quartz stabilized [22]. In the vacuum chamber, pumped with an ion and titanium sublimation pump, a base pressure of 5×10^{-11} mbar is reached. As a sample, a 10×13 mm^2 piece of a p-doped (B) silicon (111) wafer with a resistivity of $9\,\Omega$ cm is used and the 7×7-reconstruction is obtained by heating to 1300 °C for 30 s with an electron beam heater.

Typically, the experiment is started by operating the microscope in the STM mode, i.e. the feedback is controlled by the tunneling current, because the tip can be cleaned and conditioned by applying voltage pulses. The frequency shift is recorded in parallel with the topography. The tunneling current is collected at the sample and a typical setpoint of the time-averaged tunneling current is 100 pA. The surface is scanned in search for a clean spot which displays large areas of reconstructed silicon. Also, controlled collisions between tip and sample are performed in order to shape the tip such that good STM images are obtained. The frequency shift which occurs during STM imaging is used as a reference before switching into the AFM mode. Then, the tip is withdrawn and the feedback is switched to frequency shift control. The setpoint of the frequency shift is slowly decreased while the tip is scanning. While carefully decreasing the setpoint of the frequency shift, the corrugation of the image is increasing until an optimal value is reached.

One complication of AFM versus STM is that unlike in STM, the imaging signal in AFM is not monotonic with respect to distance. The tunneling current increases monotonically with decreasing tip-sample distance. However, the tip-sample force is in general attractive for large tip-sample distance and turns repulsive at a distance of the order of the equilibrium distance in the bulk crystal. Consequently, the frequency shift is also non-monotonic.

Figure 3 shows a schematic curve of a short-range tip sample interaction curve and the corresponding observable in FM-AFM – the normalized frequency shift $\gamma_{lA}(z)$-curve (see Eq. (6)). Because the feedback in an FM-AFM uses the frequency shift as the error signal, stable feedback is only possible on a monotonic branch of the frequency shift curve. When operating on the branch with positive slope, the feedback system withdraws the cantilever from the surface when the actual frequency shift is smaller (i.e. more negative) than the setpoint and vice versa. When operating at the branch with negative slope, the sign of the control output has to be reversed for obtaining proper feedback operation. The two branches meet at $z = z_{\gamma\,\mathrm{min}}$ with $\gamma(z_{\gamma\,\mathrm{min}}) = \gamma_{\mathrm{min}}$. Lüthi et al. have identified the distance range where atomic resolution is possible and found that atomic resolution is obtained for z close to $z_{\gamma\,\mathrm{min}}$ [23]. For the frequency shift curve shown in Fig. 3, stable feedback on the branch with positive slope is only possible for $z \geq 2.6$ Å. For accessing a smaller distance range, an additional long-range force can be added by applying an electric field. Hence, $z_{\gamma\,\mathrm{min}}$ is shifted to a smaller distance and tip and sample can get closer while the feedback still operates correctly. This is important for imaging atomic orbitals as evident from Fig. 8.

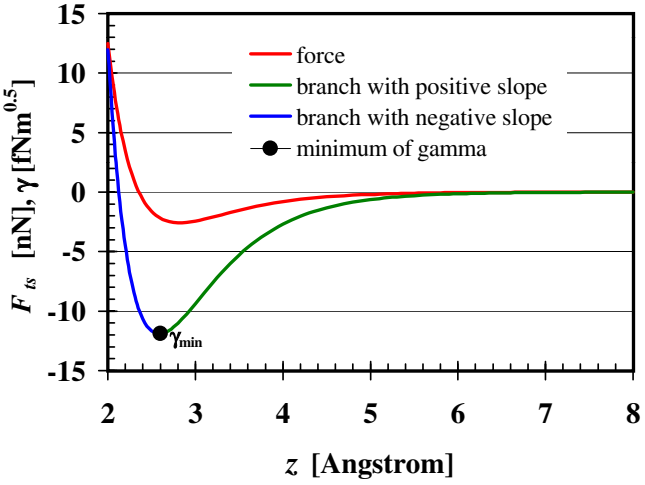

Fig. 3 Short-range force modelled by a Morse type force $F_{ts}(z) = -2E_{\text{bond}}\kappa[\exp(-\kappa(z-\sigma)) - \exp(-2\kappa(z-\sigma))]$ with $E_{\text{bond}} = 2.15\,\text{eV}$, $\sigma = 2.35\,\text{Å}$ and $\kappa = 1.5\,\text{Å}^{-1}$ and corresponding normalized frequency shift $\gamma(z)$.

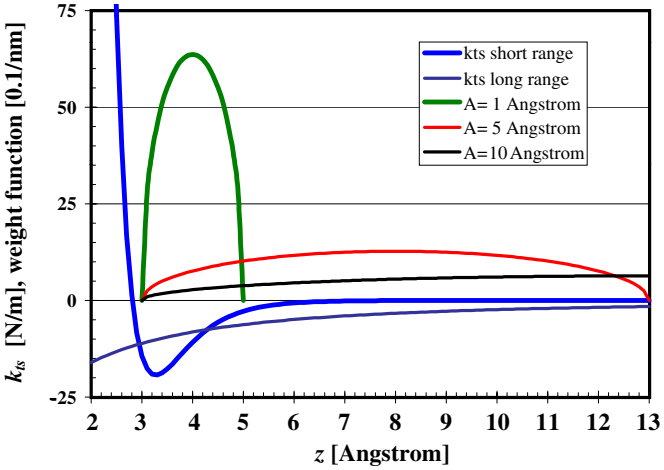

Fig. 4 Tip-sample force gradient k_{ts} and weight function for the calculation of the frequency shift.

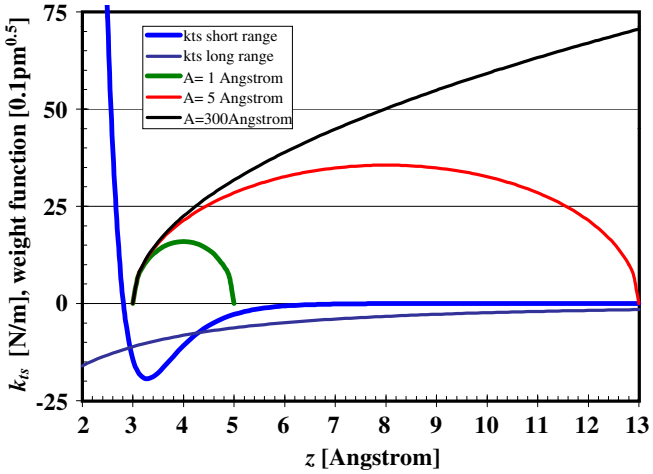

Fig. 5 Tip-sample force gradient k_{ts} and weight function for the calculation of the normalized frequency shift γ. If the amplitude A is large compared to the range of k_{ts}, the value of γ saturates and is no longer a function of A.

3 Observables in FM-AFM and physical interpretation of images

When the gradient of the tip sample forces k_{ts} is constant for the whole z range of the tip motion, the frequency shift is given by [12]

$$\Delta f(z_b) = f_0 \, \frac{1}{2k} \, k_{ts}(z_b) \tag{2}$$

where z_b is the mean z-position of the cantilever tip. If $k_{ts}(z)$ is not constant for the z-range covered by the oscillating cantilever $z_b - A < z < z_b + A$, Δf can be calculated by first order perturbation theory using the Hamilton-Jacobi approach [24]

$$\Delta f(z_b) = -\frac{f_0^2}{kA^2} \, \langle F_{ts}(z_b + q') \, q' \rangle \tag{3}$$

where z_b is the vertical base position of the cantilever as shown in Fig. 2. The precision of Δf obtained by first order perturbation theory is determined by the ratio between the magnitude of the perturbation (i.e. the tip sample potential V_{ts}) and the energy E of the oscillating CL. This ratio is in the order of 10^{-3} both in classic FM-AFM with soft cantilevers and large amplitudes ($k \approx 20\,\mathrm{N/m}$, $A \approx 10\,\mathrm{nm}$) as well as in non-contact AFM operated with very stiff cantilevers and small amplitudes ($k \approx 2000\,\mathrm{N/m}$, $A \approx 1\,\mathrm{nm}$). In both cases, the energy $E = kA^2/2$ of the cantilever is $\approx 6\,\mathrm{keV}$ while the magnitude of V_{ts} does not exceed a few eV, at least for the cases where atomic resolution is desired and the interaction between tip and sample is dominated by the front atom of the tip.

Substituting $q' = A \cos(2\pi f_0 t)$, $z = z_b - A$ yields

$$\Delta f(z) = \frac{f_0}{\sqrt{2}\,\pi k A^{3/2}} \int_0^{2A} \frac{F_{ts}(z + z')}{\sqrt{z'}} \, \frac{1 - z'/A}{\sqrt{1 - z'/2A}} \, \mathrm{d}z' \,. \tag{4}$$

Integration by parts yields an expression which is closely related to Eq. (2) [25]:

$$\Delta f(z) = \frac{f_0}{2k} \, \frac{2}{\pi A^2} \int_0^{2A} k_{ts}(z + z') \, \sqrt{2Az' - z'^2} \, \mathrm{d}z' \,. \tag{5}$$

The frequency shift is proportional to an average tip-sample force gradient, which is calculated by weighing the force gradient with a semi-circle with radius A (Fig. 4).

Thus, the use of small amplitudes increases the relative contribution of short-range forces and reduces the contribution of long-range forces to the frequency shift.

The frequency shift is a function of four parameters: k, A, f_0, and z. It is useful to exploit the scaling properties of Δf in order to be able to scale calculated frequency shifts to a variety of experimental situations. The frequency shift is strictly proportional to f_0 and $1/k$, and if A is large compared to the range of the forces (this condition is usually fulfilled, see below), it scales as $A^{-3/2}$. Therefore, it is useful to define a "normalized frequency shift"

$$\gamma(z, A) = \frac{\Delta f(z, f_0, k, A)}{f_0} \, kA^{3/2} \,. \tag{6}$$

Explicitly, we find

$$\gamma(z,A) = \frac{1}{\sqrt{2}\,\pi} \int_0^{2A} \frac{F_{ts}(z+z')}{\sqrt{z'}} \frac{1 - z'/A}{\sqrt{1 - z'/2A}}\, \mathrm{d}z' . \tag{7}$$

Again, we can integrate by parts and we find that γ is also given by the convolution of k_{ts} with a weight function:

$$\gamma(z,A) = \frac{1}{\sqrt{2}\,\pi} \int_0^{2A} k_{ts}(z+z') \sqrt{z' - \frac{z'^2}{2A}}\, \mathrm{d}z' . \tag{8}$$

If the amplitude A is large compared to the range of the tip-sample forces, the normalized frequency shift $\gamma(z,A)$ asymptotically reaches a large amplitude limit $\gamma_{lA}(z)$. This is explicitly shown for inverse power, power- and exponential forces in Ref. [26]. For Stillinger-Weber forces (see below), the deviation between $\gamma(z,A)$ and $\gamma_{lA}(z)$ is less than 3% for $A \geq 8\,\text{Å}$. For large amplitudes, we find

$$\gamma_{lA}(z) = \frac{1}{\sqrt{2}\,\pi} \int_0^{\infty} \frac{F_{ts}(z+z')}{\sqrt{z'}}\, \mathrm{d}z' = \frac{1}{\sqrt{2}\,\pi} \int_0^{\infty} k_{ts}(z+z') \sqrt{z'}\, \mathrm{d}z' . \tag{9}$$

Experimental FM-AFM images can be created in the topographic mode, where the frequency shift is kept constant and the z-position is adjusted accordingly as a function of x and y and the "constant height" mode where the frequency shift is recorded for constant z as a function of x and y. Thus, topographic FM-AFM images correspond to a three-dimensional map of $z(x,y,\gamma)$, and constant height images correspond to a three-dimensional map of $\gamma(x,y,z,A)$. Because the frequency shift of the cantilever is only a function of the z-component of the tip-sample force, $\gamma(x,y,z,A)$ is simply given by:

$$\gamma(x,y,z,A) = \frac{1}{\sqrt{2}\,\pi} \int_0^{2A} \frac{F_{ts}(x,y,z+z')}{\sqrt{z'}} \frac{1 - z'/A}{\sqrt{1 - z'/2A}}\, \mathrm{d}z' . \tag{10}$$

It is noted, that Eq. (10) implies that the cantilever vibrates exactly parallel to the surface normal vector of the sample. Conventional cantilevers have a tip which is only a few micrometers high, therefore they have to be tilted by an angle $\alpha \approx 10^\circ$ to make sure that among all the parts of the cantilever and cantilever holder, the tip is the closest part to the sample. If the cantilever is tilted around the y-axis, γ is given by

$$\gamma(x,y,z,A) = \frac{1}{\sqrt{2}\,\pi} \int_0^{2A} \frac{F_{ts}(x + q' \sin\alpha, y, z + q' \cos\alpha)}{\sqrt{q'}} \frac{1 - q'/A}{\sqrt{1 - q'/2A}}\, \mathrm{d}q' . \tag{11}$$

The qPlus sensor does not need to be tilted because it can be outfitted with large tips (see Fig. 1 in [20]) and in the simulations presented here, $\alpha = 0$ is assumed.

Dürig has devised an expanded approach for the calculation of the frequency shift which also encompasses the damping effects [27].

4 Calculation of tip-sample forces

The first step for the simulation of images is the calculation of the tip sample forces F_{ts}. One approach for this task is the use of the density functional theory and related methods, such as shown by Perez et al. [15]. However, as emphasized by Bazant et al. [28] the use of empirical force models still has its merits, because *ab initio* methods require much more computing power and programming effort than the use of empirical force models. Here, we estimate the force between the tip of a cantilever and a flat sample $F_{ts}(x, y, z)$ by a long-range component that is only a function of vertical tip-sample distance z and a short-range force that also depends on the lateral coordinates x and y:

$$F_{ts}(x, y, z) = F_{lr}(z) + F_{sr}(x, y, z)\,. \tag{12}$$

4.1 Van-der-Waals forces

In principle, the van-der-Waals (vdW) force is a short-range force, characterized by the $1/r^6$ vdW potential. However, the vdW force between two individual atoms is weak compared to the chemical and electrostatic short-range forces. Nevertheless, the total vdW force between a typical AFM tip and a flat sample can be substantial. When assuming that the vdW force is additive, the sum over the individual pair contributions can be replaced by an integration over the volume of the tip and sample (Hamaker integration) [29, 30]. For a spherical tip with radius R, the vdW force is given by

$$F_{\mathrm{vdW}}(\zeta) = -\frac{A_H R}{6\zeta^2} = \frac{C_{\mathrm{vdW}}}{\zeta^2} \tag{13}$$

where A_H is the Hamaker constant and ζ is the distance between the center of the front atom of the tip and the plane connecting the centers of the top layer of the sample atoms. For a Si tip and a Si sample, $A_H = 0.186\,\mathrm{aJ}$ [31]. The corresponding normalized frequency shift is [26, 32]

$$\gamma_{\mathrm{vdW}}(\zeta, A) = \frac{1}{(2 + \zeta/A)^{3/2}}\,\frac{C_{\mathrm{vdW}}}{\zeta^{3/2}}\,. \tag{14}$$

4.2 Chemical bonding forces

If tip and sample consist of silicon, the Stillinger-Weber (SW) potential [33] can be used to model the chemical interaction. As noted by Bazant et al. [28], the SW potential is a fairly good model for the mechanical properties of silicon. The SW potential has been used before for the simulation of AFM images of Si(001)-(2×1) in the quasistatic mode by Abraham et al. [34].

The SW potential necessarily contains nearest and next nearest neighbor interactions. Unlike solids with a face centered cubic or body centered cubic lattice structure, solids which crystallize in the diamond structure are unstable when only next-neighbor interactions are taken into account. The nearest neighbor contribution of

the SW potential is

$$V_n(r) = E_{\text{bond}} A \left[B \left(\frac{r}{\sigma'}\right)^{-p} - \left(\frac{r}{\sigma'}\right)^{-q}\right] \exp\left(\frac{1}{r/\sigma' - a}\right) \quad \text{for} \quad r < a\sigma',$$
$$= 0 \quad \text{for} \quad r > a\sigma'. \tag{15}$$

The next nearest neighbor contribution is

$$V_{nn}(\mathbf{r}_i, \mathbf{r}_j, \mathbf{r}_k) = E_{\text{bond}}[h(r_{ij}, r_{ik}, \theta_{jik}) + h(r_{ji}, r_{jk}, \theta_{ijk}) + h(r_{ki}, r_{kj}, \theta_{ikj})] \tag{16}$$

with

$$h(r_{ij}, r_{ik}, \theta_{jik}) = \lambda \exp\left(\frac{\gamma}{r_{ij}/\sigma' - a} + \frac{\gamma}{r_{ik}/\sigma' - a}\right)\left(\cos\theta_{jik} + \frac{1}{3}\right)^2 \quad \text{for} \quad r_{ij,ik} < a\sigma'$$
$$= 0 \quad \text{for} \quad r_{ij,ik} > a\sigma'. \tag{17}$$

Stillinger and Weber found optimal agreement with experimental data for the following parameters:

$$A = 7.049556277 \qquad p = 4 \qquad \gamma = 1.20$$
$$B = 0.6022245584 \qquad q = 0 \qquad \lambda = 21.0$$
$$E_{\text{bond}} = 0.34723\ \text{aJ} \qquad a = 1.8 \qquad \sigma' = 2.0951\ \text{Å}.$$

The equilibrium distance σ is related to σ' by $\sigma = 2^{1/6}\sigma'$. The potential is constructed in such a way to ensure that V_n and V_{nn} and all their derivatives with respect to distance vanish for $r > a\sigma' = 3.7718\,\text{Å}$. The diamond structure is favoured by the SW potential because of the factor $(\cos\theta + \frac{1}{3})^2$ – this factor is zero when θ equals the tetrahedon bond angle of $\theta_t = 109.47°$. The SW potential leads to a maximal chemical contribution to the normalized frequency shift of $\gamma \approx -10\,\text{fNm}^{1/2}$. This has been verified with great precision in an experiment where the electrostatic interaction was carefully minimized by Lantz et al. [35, 36]. Recently, Laschinger has performed tight binding calculations for a silicon tip and a silicon sample [37] and has also found a double peak in γ with a magnitude of $\gamma \approx -10\,\text{fNm}^{1/2}$. However, the distance at which this double peak occurs is much higher in the tight binding calculation than in the SW result.

4.3 Electrostatic forces

The electrostatic force for a spherical tip with radius R at a differential voltage U with respect to a flat surface at distance ζ is given by [38]

$$F_{lr\,\text{est}}(\zeta) = -U^2 \pi \epsilon_0 \frac{R}{\zeta} = \frac{C_{\text{est}}}{\zeta}, \tag{18}$$

for $R \gg \zeta$, where U is the bias voltage between tip and sample. This formula is only correct for $\zeta \gg \sigma$ where σ is the nearest neighbor distance in the bulk material of tip and sample. The corresponding normalized frequency shift is [26, 32]

$$\gamma_{\text{est}}(\zeta, A) = \frac{C_{\text{est}}}{\sqrt{2\zeta}} \left(\frac{1 + \zeta/A}{\sqrt{1 + \zeta/(2A)}} - \sqrt{\frac{2\zeta}{A}}\right). \tag{19}$$

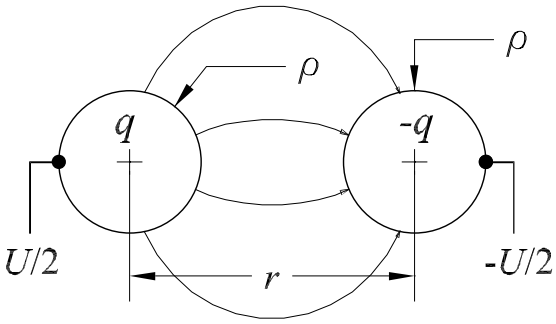

Fig. 6 Electrostatic interactions of two spheres with radius ρ and distance r at a voltage differential U.

For a very small tip-sample distance, there will also be short-range electrostatic forces. The electrostatic potential is very large close to the nuclei of the atoms, and because the electrons shield this field, the electrostatic potential decays exponentially (see Eq. (22)). If a bias voltage U is applied between tip and sample, surface charges will result and the electrostatic field has a component which decreases exponentially with the surface separation with a decay length $\lambda = \sigma/(2\pi)$ [39]. If a bias U is applied between tip and sample, we can roughly estimate the charge that is induced in the tip and sample atom with the image charge method. We treat both tip and sample atom as a conducting sphere with radius ρ at a distance between their centers of r. What is the charge induced on the spheres if we vary r and keep the voltage differential U constant? The voltage differential at the two spheres leads to an induced charge in the spheres which is approximately given by

$$q(r) = 2\pi\epsilon_0 U\rho\left(1 + \frac{\rho}{r - 2\rho}\right). \tag{20}$$

This follows from an electrostatic analogy: the equipotential surface of a point charge is a sphere, and for two charges separated by r, the equipotential surfaces again are approximately spherical. If we model the front atom of the tip and the sample atom closest to the tip by a sphere with electrostatic potential $U/2$ and $-U/2$ respectively, we can estimate the potential energy by

$$V_{sr\,\mathrm{estatic}}(r) = -\pi\epsilon_0 U^2\rho^2\left(1 + \frac{\rho}{r - 2\rho}\right)^2 \frac{1}{r}. \tag{21}$$

Hence, the force is given by $F_{sr\,\mathrm{estatic}} = -\partial V_{sr\,\mathrm{estatic}}/\partial z$ with $r = \sqrt{x^2 + y^2 + z^2}$. The total electrostatic force is then calculated by summing a long-range electrostatic force of a tip with a tip radius R according to Eq. (18) and a short range force given by the short range potential after Eq. (21). This model is shown in Fig. 7. We can thus estimate the electrostatic force by a long-range contribution caused by the interaction of a macroscopic tip with radius R with a flat surface plus a short-range contribution describing the interaction of the front atom with the sample atom closest to it.

The model of atoms as perfectly conducting spheres is certainly only a rough approximation. When getting down to atomic length scales, the induced charges will not spread over the surface of a sphere with the atomic radius. Instead, the

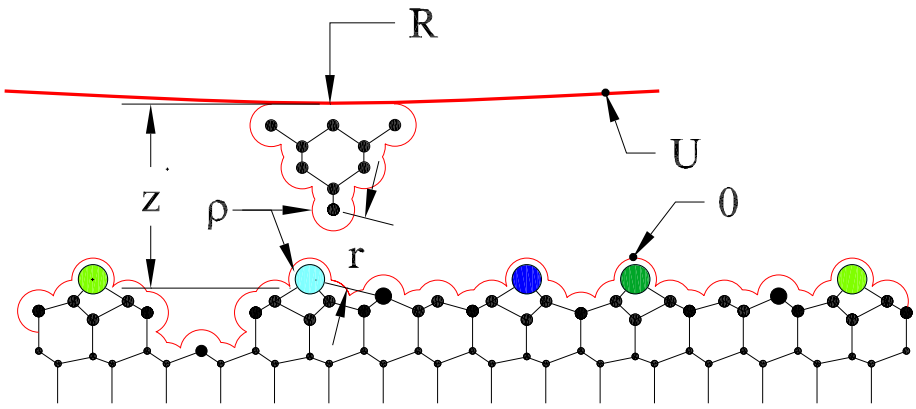

Fig. 7 Electrostatic interactions of a macroscopic tip with a radius R plus a front atom with radius ρ at a voltage differential U.

induced charges will modify the filling of the electronic states at tip and sample at the Fermi energy, i.e. the valence orbitals. Therefore, we first take a look at the charge density of the valence states in silicon. The electronic wave functions of the valence shell of atoms can be approximately constructed with the use of the Slater-type orbital model [40]. The radial functions of the wave function are given by

$$f_{nl}(r) = \frac{N_{nl}}{a_B^{3/2}} \left(\frac{r}{a_B}\right)^{n-1} \exp\left(-\frac{Z_e r}{n a_B}\right). \tag{22}$$

where n is the main quantum number, N_{nl} is a normalization constant, $a_B = 0.529\,\text{Å}$ is Bohr's radius and $Z_e = Z - s$ where Z is the nuclear charge and s is a screening constant. For the valence shell of silicon, $n = 3$, $Z = 14$ and $s = 9.85$ according to the procedure described in Ref. [40]. The normalization constants are given by

$$N_{30} = \sqrt{\frac{2}{45\pi}} \left(\frac{Z_e}{n}\right)^{7/2} \quad \text{and} \quad N_{31} = \sqrt{\frac{2}{15\pi}} \left(\frac{Z_e}{n}\right)^{7/2}. \tag{23}$$

The wave functions corresponding to the four $3sp^3$ orbitals are constructed by

$$\begin{aligned}
|\psi_1(x,y,z)\rangle &= \tfrac{1}{2}\left[f_{30}(r) + f_{31}(r)\,(+x/r + y/r + z/r)\right], \\
|\psi_2(x,y,z)\rangle &= \tfrac{1}{2}\left[f_{30}(r) + f_{31}(r)\,(-x/r - y/r + z/r)\right], \\
|\psi_3(x,y,z)\rangle &= \tfrac{1}{2}\left[f_{30}(r) + f_{31}(r)\,(+x/r - y/r - z/r)\right], \\
|\psi_4(x,y,z)\rangle &= \tfrac{1}{2}\left[f_{30}(r) + f_{31}(r)\,(-x/r + y/r - z/r)\right].
\end{aligned} \tag{24}$$

The maximal charge density occurs at a radius where $r^2 f_{nl}^2(r)$ is maximal, i.e. for

$$r_{\max} = a_B \frac{n^2}{Z_e}. \tag{25}$$

For silicon with $n = 3$, $r_{\max} = 1.147\,\text{Å}$, close to $\sigma/2 = 1.175\,\text{Å}$ where σ is the next neighbor distance in the bulk. In our estimate of the electrostatic short-range inter-

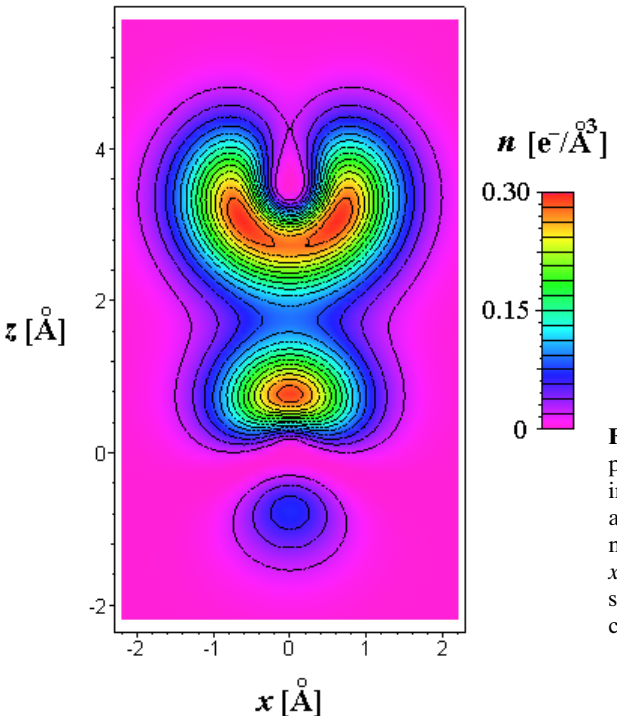

Fig. 8 Charge density (in electrons per Å^3) for one $3sp^3$ orbital originating from an adatom located at $x = 0$ and $z = 0$ and two $3sp^3$ orbitals originating from a tip atom located at $x = 0$ and $z = 3.5$ Å. The mean density of valence electrons in bulk silicon is 0.2 electrons per Å^3.

action, we assume that the induced charge is centered around the maximum of the charge distribution at $r_{max} = 1.147$ Å with a radius $\sigma/2$. Figure 8 shows the calculated charge density. This figure shows, that in order to observe two separate maxima of the charge density in an xy-plane, the z-distance of tip and sample atom

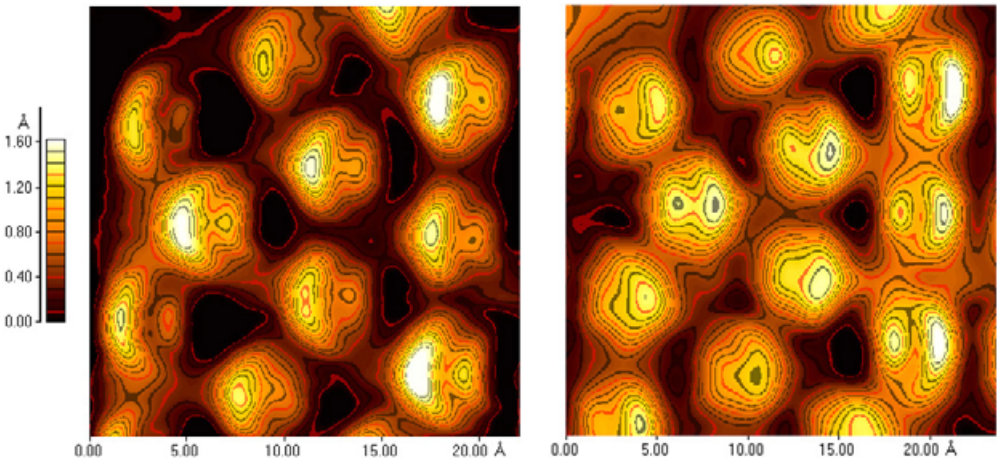

Fig. 9 Topographic image of Si(111)-(7 × 7) observed by FM-AFM, presumably imaged with a (001) oriented Si tip. Imaging parameters: $k = 1800$ N/m, $A = 8$ Å, $f_0 = 16860$ Hz, $\Delta f = -160$ Hz, rms frequency error $\delta\,\Delta f = 9$ Hz, scanning speed = 80 nm/s, sample voltage $U = 1.6$ V.

needs to be extremely small. Thus, imaging both dangling bonds separately is only possible if the minimal tip sample distance is of the order of the nearest neighbor distance of the atoms in the bulk crystal. The calculation of the charge density does not take the interaction of the adatom and the tip into account. Because of Pauli's exclusion principle, the adatom can only form a bond to one of the tip dangling bonds at the same time.

The long-range forces described with the models above vary strongly with the macroscopic tip shape, and the short-range forces are a function of the chemical identity of the front atom and its alignment to its bonding partners in the tip. Once we have learned to prepare the AFM tip in a well defined manner such that we know the atomic arrangement and chemical identity of the tip apex, precise calculations of the tip-sample force are highly desirable.

5 Experimental results and simulations

Figure 9 shows an experimental result of a Si(111)-(7×7) surface observed by FM-AFM. Every adatom appears to have two peaks. This feature has been attributed to two dangling bonds originating at the tip which image the single dangling bond of the adatoms. While this image was recorded with a tungsten tip, we think that the tungsten tip had a silicon crystallite or cluster at its end. The notion, that tungsten tips pick up silicon such that the front atom is made of silicon has been put forth in STM experiments before [41–43]. This interpretation of the data has been challenged recently [44]. We could show, that the feedback issues proposed are not relevant in our experiment [45]. Further, the asymmetry between the two scan directions is not due to a finite feedback speed, but must be caused by elastic tip deformations such as illustrated in Figure 10. Figure 11 shows a magnified view of a single adatom. The distance between the contour lines is 10 pm, so the left peak is about 60 pm higher than the right peak and the depth between the peaks is approximately 20 pm. Using Eq. 10, we can calculate the expected image once we know the tip-sample force. As we have noted in Ref. [24], a qualitative picture can be simulated from a long-range vdW force and a short range chemical force given

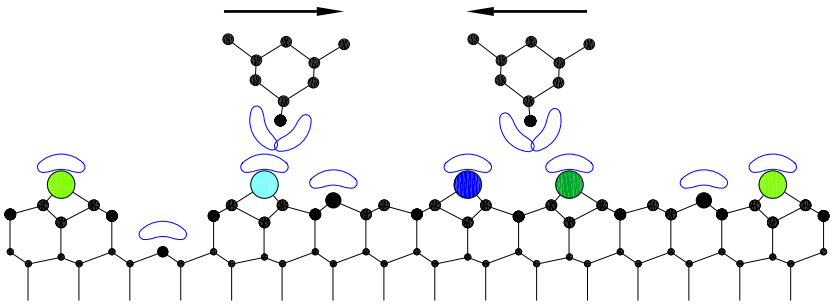

Fig. 10 Tip bending effect: For a tip crystallite with the geometry proposed, the stiffness in scanning (x) direction is very small so it is likely that the tip apex bends opposite to the scan direction. This bending explains the reversal in the height of the two adatom peaks when the scanning direction reverses (Fig. 9).

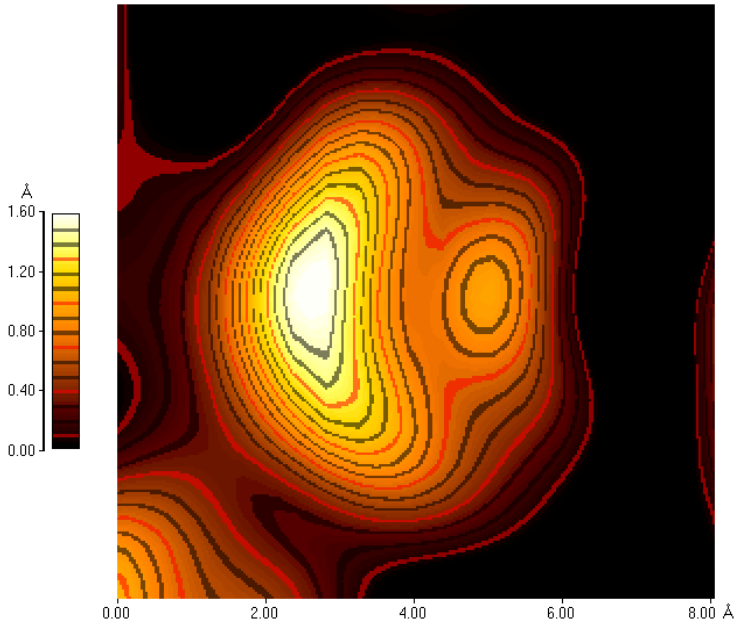

Fig. 11 Topographic image of a single adatom on Si(111)-(7 × 7) observed by FM-AFM, presumably imaged with a (001) oriented Si tip. The following imaging parameters were used: $k = 1800\,\mathrm{N/m}$, $A = 8\,\text{Å}$, $f_0 = 16860\,\mathrm{Hz}$, $\Delta f = -160\,\mathrm{Hz}$, rms frequency error $\delta\,\Delta f = 9\,\mathrm{Hz}$, scanning speed = 80 nm/s, sample voltage $U = 1.6\,\mathrm{V}$, scanning direction: left to right.

by the SW potential. Fig. 12 shows the result of that calculation. The left image is simulated for the experimental normalized frequency shift according to Figure 11 where $\gamma = -160\,\mathrm{Hz}/16860\,\mathrm{Hz} \times 1800\,\mathrm{N/m} \times (8\,\text{Å})^{3/2} = -387\,\mathrm{fNm}^{1/2}$. The double

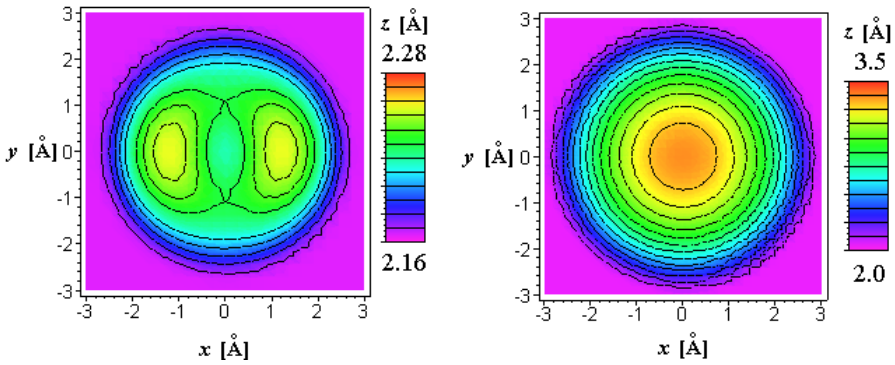

Fig. 12. Simulation of a topographic FM-AFM image of a single adatom on Si(111)-(7 × 7). Parameters (Left): $\gamma = -387\,\mathrm{fNm}^{1/2}$, $A = 8\,\text{Å}$, short-range force: Stillinger Weber, tip geometry shown in Fig. 17, long-range force = $-3.66 \times 10^{-26}\,\mathrm{Jm}/(z + \Delta)^2$, $\Delta = 5$ Å. Parameters (Right): $\gamma = -4\,\mathrm{fNm}^{1/2}$, $A = 8\,\text{Å}$, short-range force: Stillinger Weber, tip geometry shown in Fig. 17, long-range force = $-3.66 \times 10^{-28}\,\mathrm{Jm}/(z + \Delta)^2$, $\Delta = 5$ Å.

peaked adatom image can only occur if the long-range attractive force is strong enough such that $\gamma_{\min}$ occurs at a distance where the charge density of the tip shows strong lateral variations. The right image is simulated for $\gamma = -4\,\mathrm{fNm}^{1/2}$ – a typical value for weak vdW attractive forces [35, 36]. The left and the right images are simulated with a Si tip which exposes two dangling bonds (see Fig. 17). However, the two dangling bonds appear separated only if the long-range attractive force is strong enough to allow imaging at very small distances. Several approximate procedures for obtaining $\gamma(x, y, z)$ which are numerically much less expensive than the exact calculation after Eq. (10) have been proposed:

1. Ke et al. [46] found that under certain conditions, the geometric mean between force and energy is roughly proportional to the frequency shift;
2. Schwarz et al. [47] propose to approximate γ by $\gamma \approx \frac{\sqrt{2}}{\pi} \frac{V_{ts}}{\sqrt{\lambda}}$ where λ is the range of the tip sample potential V_{ts};
3. In an earlier publication [26] we proposed to decompose the tip-sample interaction into monotonic basic types F_{ts}^i with an exponential-, power- or inverse power- z-dependence and showed that $\gamma \approx \frac{1}{\sqrt{2\pi}} \sum_i F_{ts}^i \sqrt{V_{ts}^i / F_{ts}^i}$.

However, as pointed out by Hölscher et al. [48], the use of the approximative approaches leads to inaccuracies for small tip-sample distances. Moreover, method 1 predicts that $\gamma(\xi) = 0$ for $V_{ts}(\xi) = 0$ and $F_{ts}(\xi) = 0$ and method 2 predicts that $\gamma(\xi) = 0$ for $V_{ts}(\xi) = 0$ which is incorrect. Because we are simulating images at very small tip-sample distances we refrain from using the approximate procedures and perform the integration of γ after Eq. (10). The integration is implemented with Newton's method – a step width of 5 pm has proven to provide sufficient accuracy.

Qualitatively, the calculated image in Fig. 12 (left) is similar to the experimental image in Fig. 11. However, the adatom height in the calculated image is only 0.12 Å – a tenth of the experimental height. This is because the electrostatic short range interaction has been neglected. The relevance of the electrostatic short-range force is confirmed by experimental results of atomic resolution on silicon with an applied bias voltage where the normalized frequency shift has reached magnitudes as high as $-180\,\mathrm{fNm}^{1/2}$ [23] and even $-500\,\mathrm{fNm}^{1/2}$ [49].

In Figure 13, we have also taken the short-range electrostatic force into account. Because we have approximated the charges of the dangling bonds to concentrate on a point, the simulated adatom image shows two spherical subpeaks – in contrast to the crescent shaped experimental subpeaks. We expect that if accurate charge distributions were taken into account, crescent shaped simulated images would result. The height of the simulated adatoms, the distance of the subpeaks and the dip between the subpeaks is in excellent agreement with the experimental images.

Since our first observation of subatomic features by AFM, we have observed similar images of double peaked adatom structures in various other experiments. In our first experiments, the orientation of the double peaks was roughly perpendicular to the fast scanning direction. In Figure 14 we present examples of AFM data where the orientation of the crescents is clearly unrelated to the fast scanning direction.

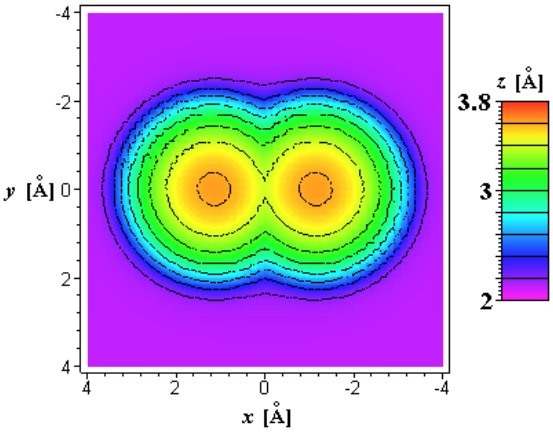

Fig. 13 Simulation of a topographic FM-AFM image of a single adatom on Si(111)-(7 × 7). Parameters: $\gamma = -387\,\mathrm{fNm}^{1/2}$, $A = 8\,\text{Å}$, $U = 1.6\,\mathrm{V}$, short-range electrostatic force after Eq. 21, tip radius $R = 1000\,\text{Å}$, Hamaker constant $A_H = 0.4\,\mathrm{aJ}$, van der Waals force = $-A_H \times R/(6(z+\Delta)^2)$, $\Delta = 2\,\text{Å}$, long-range electrostatic force = $U^2\pi\epsilon_0 R/(z+\Delta-\sigma)$.

Because of the dramatic dependence of the images on the atomic tip state, the preparation of AFM tips with a specified front atom symmetry and chemical identity is instrumental for performing well defined experiments. Commercial silicon cantilever tips are oriented in a (001)-direction. In silicon, the natural cleavage planes are (111) planes. If a macroscopic tip crystallite is limited by natural cleavage planes, a (001) oriented tip will in general not end in a single atom tip, but in

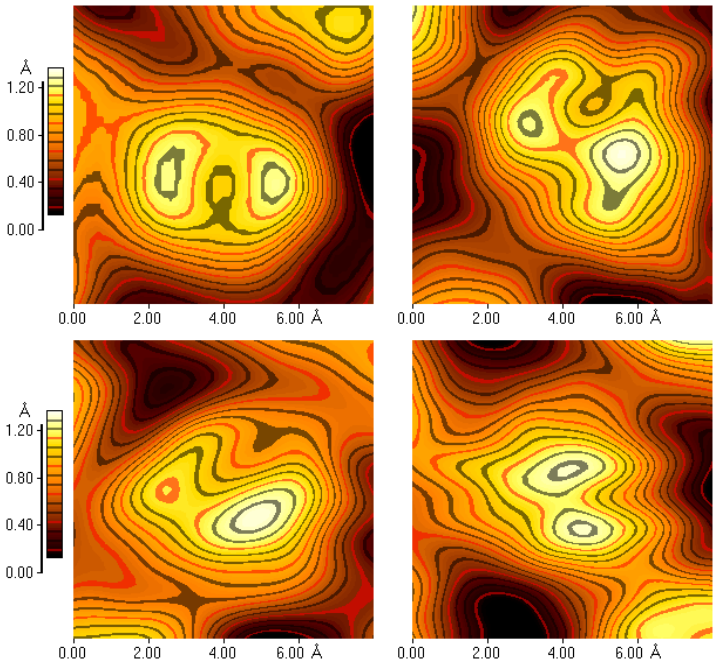

Fig. 14. Experimental FM-AFM images of adatoms exposing two peaks per atom. In all the images, the fast scanning direction is horizontal (x). The orientation of the double peaks is clearly unrelated to the fast scanning direction.

a rooftop type of symmetry. A tip which points into a (111)-direction, however, will end in a single atom if we assume bulk termination. Moreover, the front atom of this tip is expected to be particularly stable, because it is bonded to the rest of the tip by three bonds and exposes a single dangling bond towards the sample. Because of this prospects, we have attempted to cleave single crystalline silicon such that we obtained crystallites which were limited by (111) planes supposedly ending in a single atom tip [50]. We have cleaved the silicon in air, so that an oxide layer of a typical thickness of 20 Å will develop at the surface. As expected, the tips did not yield good STM images after bringing them into vacuum. However, after exposing them to electron bombardment (the same procedure is used for preparing the silicon 7×7 surface), the tips work excellently in STM mode and also in AFM mode. We speculate, that the (111) oriented sidewalls of the tip will reconstruct just like a flat silicon surface. Even then, the front atom will be bonded to three next neighbors and expose a single dangling bond. Figure 15 shows an AFM image obtained with such a (111) oriented tip. It is also noted, that this image was recorded at *positive* frequency shift. Hence, the forces between front atom and sample have been repulsive! An advantage of this mode is that the feedback can be set much faster, because the risk of feedback oscillations with a catastrophic tip crash is avoided in this mode. Due to the faster feedback setting and

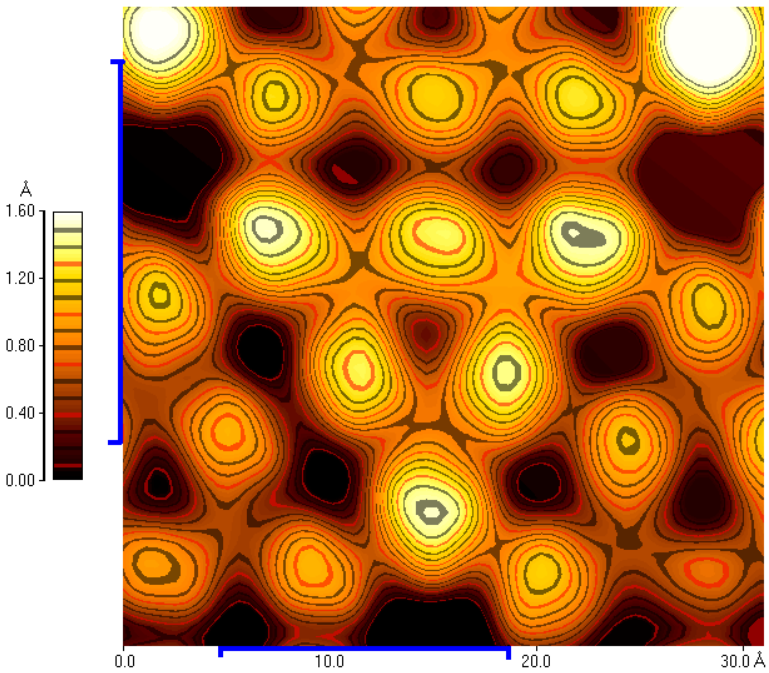

Fig. 15 Topographic image of Si(111)-(7×7) observed by FM-AFM, imaged with a single crystal silicon tip roughly oriented in a (111) direction. Imaging parameters: $k = 1800$ N/m, $A = 2.5$ Å, $f_0 = 20531$ Hz, $\Delta f = +85$ Hz, thus $\gamma = +30\,\mathrm{fNm}^{1/2}$, rms frequency error $\delta\,\Delta f = 0.09$ Hz, scanning speed = 20 nm/s. The blue bars at the left and bottom border of the image indicate the x, y-range that is simulated in Fig. 16.

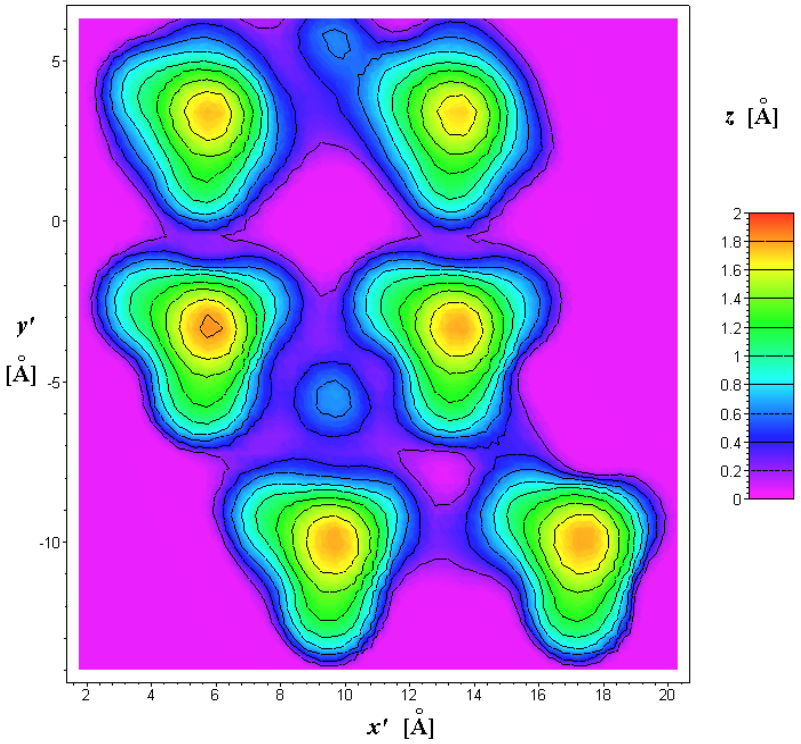

Fig. 16 Simulated image of a section of the unit cell showing for $\gamma = +30\,\mathrm{fNm}^{1/2}$. All four types of adatoms as well as the rest atoms are visible, imaged with a silicon crystallite oriented in a (111) direction with a front atom with a single dangling bond. The Stillinger-Weber potential has been used for the calculation of the image. The positions of the surface atoms are adapted from Tong et al. [51].

the smaller scanning speed, the relative rms frequency error ($= \delta\,\Delta f/\Delta f$) is significantly smaller in Fig. 15 (0.1%) than in Fig. 9 (5.6%). Figure 16 shows the simulated image. Because the forces are repulsive, the dominant forces are modelled with the repulsive part of the SW potential.

6 Discussion

The experimental data which is presented here confirms the prediction of Eq. (1): the resolution of the AFM is improved by working at small oscillation amplitudes. The resolution obtained in the AFM images is high enough such that the angular dependence of the tip-sample forces is revealed. Chemical and electrostatic force models have been employed to explain and analyze the experimental images. The choice of our model forces leads to a qualitative agreement between experiment and simulations. The double peak images are well explained by a SW potential and additional electrostatic effects which polarize the orbitals. However, using only the SW potential for the short-range contribution results in a simulated height of

the adatoms which is only 10 % of the experimental value. Adding the simple electrostatic short-range interaction, the height of the simulated adatoms agrees well with experiment, while the shape of the adatom images differs from experiment. The experimental images show crescents, while the theoretical images are spherical. It is apparent that the simulation of the images captures the basic principle, but needs to be refined for obtaining a better agreement with experiment.

The simulations covering the repulsive regime with a SW potential leads to a qualitative agreement between experiment and simulations. The simulation shows that the rest atoms, located between a corner adatom and two center adatoms, should be visible as a small protrusion. The experiment shows a saddlepoint at the expected rest atom positions and a hole between three center adatoms. However, the shape of the four types of adatoms is similar in the simulation and very different in the experiment which shows that taking only next neighbor interaction and bond angles into account is insufficient for a proper model of the forces between silicon atoms. Also, the heights of the adatoms is much different than measured by LEED or predicted by calculations [52]. According to LEED data, the corner adatoms are only about 0.04 Å higher than the center adatoms. In our AFM data, the corner adatoms appear to be roughly 0.2 Å higher than the center adatoms. Because this height difference is measured both with repulsive and attractive short-range forces, it cannot be caused by elastic deformations of tip and sample.

Our simulations have shown, that the observation of atomic orbitals is only possible if the tip-sample distance is of the order of the interatomic distance in the bulk material. The forces that act for such small distances are large, and deformations and increased dissipation are expected to occur. These issues and the observability of atomic orbitals by STM are discussed in the following subsections.

6.1 Tip stability issues

An important issue arises in the tip and sample stability. So far, we have assumed that both tip and sample atoms are not strained when the tip comes close to the sample. In STM, this might be the case when the tunneling impedance is large, and even in dynamic AFM it is conceivable that F_{ts} is small enough such that the elastic deformation of tip and sample is not noticeable.

However, as is evident from Fig. 8, the observation of deviations of the spherical symmetry of atoms is only possible in the near field, i.e. for distances which are of the order of the bulk interatomic distance. Thus, for observing these features by AFM, tip and sample have to come very close, and the atoms close to the interaction region will suffer from noticeable strain. Figure 17 shows a ball and stick model of a silicon crystallite which is limited by (111) planes and points into a (001) direction. This crystallite is used as a model for our tip.

The stiffness of the bonds of the front atom to the upper part of the tip can be estimated using the Stillinger-Weber potential. For the crystallite shown in Fig. 17, the stiffness in z-direction is 115 N/m, in x-direction it is 20.4 N/m and in y-direction it is 224 N/m. The stiffness can also be evaluated from the phonon spectrum of silicon. For an optical phonon at the Γ-point (i.e. the wave vector is zero), neighboring atoms vibrate opposite to each other. We can model this situation with a single silicon atom which is suspended by four springs with half the length of the

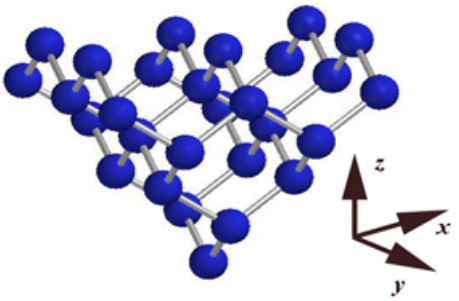

Fig. 17 Model for a tip crystallite cleaved from bulk silicon with (111)-oriented surfaces and pointing in a (001) direction.

nearest neighbor distance, each having an effective spring constant in z-direction of $k_{z\,\mathrm{half\,bond}}$. The wave number of optical phonons in silicon at the Γ-point is $520\,\mathrm{cm}^{-1}$ which corresponds to $f_{\mathrm{opt.\,phonon}} \approx 15.589\,\mathrm{THz}$ [2]. The mean atomic mass (natural mixture of isotopes) of silicon is 28.086 amu [51], thus the spring constant $k_{z\,\mathrm{half\,bond}} = \frac{1}{4} \times 447.45\,\mathrm{N/m} = 111.9\,\mathrm{N/m}$. The stiffness of the two bonds connecting the front atom of the tip crystallite with the rest of the tip is given by twice the stiffness of one full-length bond with $k = \frac{1}{2}\, k_{z\,\mathrm{half\,bond}}$ yielding $k_z = 111.9$ N/m – in excellent agreement with the value of 115 N/m derived from the Stillinger-Weber potential.

The positions of the two atoms which attach to the front atom have been kept fixed for the derivations. In reality, all the tip atoms will respond to the force on the front atom. The effect can be estimated by arranging the springs corresponding to a tip atom layer in series. For the tip shown in Fig. 17, the m-th bilayer contains one layer with m^2 and one layer with $m(m+1)$ atoms. Each of these atoms has two bonds to the layer above. The effective stiffness of the tip crystallite in z-direction is then given by

$$\frac{1}{k_{\mathrm{eff}}} = \frac{1}{k_z} \sum_{m=1}^{\infty} \left[\frac{1}{m^2} + \frac{1}{m(m+1)} \right] = \frac{1}{k_z} \left(1 + \frac{\pi^2}{6} \right) \approx \frac{1}{0.4 \cdot k_z} \,. \tag{26}$$

For tip-sample forces of the order of 2 nN, we expect that the bonds between the front atom of the tip and its next neighbors will be strained by $2\,\mathrm{nN}/k_z \approx 0.2$ Å. The total strain of the tip is expected to be $2\,\mathrm{nN}/k_z/0.4 \approx 0.5$ Å. It is expected that the sample will become strained to a similar extent.

6.2 Amplitude feedback stability

When the oscillating cantilever of an FM-AFM comes close to the sample, increased damping has been observed experimentally [49, 53–55] and described theoretically [13, 27, 56–59].

We expect that in addition to the damping channels which are present in classic FM-AFM, an even more significant damping channel will open up for very small tip sample distances. When the front atom of the tip moves to the sample, both the front atom and the adjacent sample atom will be pulled from their equilibrium position and relax when the cantilever swings back from the sample. This process will happen adiabatically and dissipate little energy as long as the closest distance is larger than the distance where the maximal attractive force $F_{\mathrm{att\,max}}$ occurs (inflection point).

However, when the distance between front atom and sample gets closer than the inflection point, an additional channel of significant energy loss will occur because the front atom of the tip and the sample atom will be pulled out of the equilibrium position, and rather than moving back adiabatically, will stick together until the bonding force is overcome by the withdrawing cantilever. At this point, the front atom and the sample atom will be pulled out by a distance $F_{\text{att max}}/k_z$. When the cantilever swings back, the front and sample atom will oscillate at the phonon frequency and dissipate the stored energy

$$\Delta E = \frac{F_{\text{att max}}^2}{2\,k_z}\,. \tag{27}$$

Recently, a similar dissipation process has been described by Sasaki and Tsukada [59]. The maximal attractive force $F_{\text{att max}}$ is about 4 nN, according to the SW potential. Thus, the energy loss per cycle due to this process is 0.08 aJ per atom. Because both the front atom at the tip and the sample atom will be excited by this process, the total energy loss is thus of the order of 1 eV per cycle. This energy has to be provided by the oscillator circuit which drives the cantilever. The intrinsic energy loss of the cantilever is $\pi k A^2/Q$, where k is the spring constant of the cantilever, A is its oscillation amplitude and Q is its quality factor. For the qPlus sensor, $Q \approx 4000$ and $k = 1800$ N/m. For an amplitude of the order of 1 nm, the intrinsic loss per cycle is of the order of 10 eV and the extra loss due to tip-sample dissipation is small. With conventional silicon cantilevers, typical Q factors are at least one order of magnitude larger and the intrinsic dissipation is much smaller. Amplitude control can become difficult with conventional cantilevers when attempting to get very close to the sample as required for observing the orbital structure of atoms.

6.3 Observability of individual orbitals by STM

To our knowledge, the observation of multiple maxima in the image of a single atom in STM mode has not been reported before. We can identify three possible explanations why the internal orbital electron structure of atoms is observable by AFM, but apparently not by STM:

1. As shown in Fig. 8, the tip sample distance needs to be very small before the charge density of valence electrons displays a noticeable deviation from the rotational symmetry about the z-axis. Typical tip-sample distances (from the center of the tip atom to the center of the closest sample atom) are 5–8 Å in STM. When attempting to image in STM mode at a tip sample distance of 2–3 Å, the tip-sample force is very large and the tip atom or sample atom may not withstand the shear forces acting during scanning. In dynamic AFM, this small distance occurs only intermittently and the lateral movement can occur during the oscillation phase where the tip is far from the sample;
2. While it is known that the force between two atoms is in general attractive at large distances and becomes repulsive at short distances, the tunneling current is usually assumed to be a monotonic function of the distance. Thus, it is expected that the orbital structure of the valence electrons has a larger effect on the force than on the tunneling current;

3. In the STM mode, typical tunneling voltages used for imaging silicon are of the order of 2 V and the energy of the tip and sample states which contribute to the tunneling current is spread over a range of 2 eV. Just like in atomic wave functions, where the angular dependent p, d and f sub-shells add up to a spherically symmetric charge distribution if all the states of a given main quantum number are filled, we expect that a similar process can happen in tunneling experiments when a range of tip and sample energies contributes to the total tunneling current. So it is conceivable that even if some states which contribute to tunneling are not symmetric with respect to the z-axis, the sum of these states is symmetric around z.

In summary, we have shown that atomic force microscopy offers new insights into the atomic structure and symmetry of surface atoms and AFM tips. We are confident that using small oscillation amplitudes, stiff cantilevers and oscillator setups which are insensitive to the enhanced damping at very close tip-sample distances provides a new experimental tool to study the nature of the atomic bond and the electronic structure of atoms.

The authors wish to thank M. Herz, H. J. Hug, T. Kopp, M. Lantz, and C. Laschinger for fruitful discussions. This work is supported by the BMBF (project no. 13N6918/1).

References

[1] R. E. Schlier and H. E. Farnsworth, J. Chem. Phys. **30** (1959) 917
[2] Landolt-Börnstein, p. 370, Numerical Data and Functional Relationships in Science and Technology, Vol. 17a, edited by O. Madelung, M. Schultz, and H. Weiss, Springer, Berlin 1982
[3] G. Binnig, H. Rohrer, Ch. Gerber, and E. Weibel, Phys. Rev. Lett. **50** (1983) 120
[4] K. Takayanagi, Y. Tanishiro, and S. Takahashi, J. Vac. Sci. Technol. A **3** (1985) 1502
[5] G. Binnig, C. F. Quate, and Ch. Gerber, Phys. Rev. Lett. **56** (1986) 930
[6] L. Howald, R. Lüthi, E. Meyer, and H.-J. Güntherodt, Phys. Rev. B **51** (1995) 5484
[7] F. J. Giessibl, Science **267** (1995) 68
[8] S. Kitamura and M. Iwatsuki, Jpn. J. Appl. Phys. **34** (1995) L145
[9] Proceedings of the First International Workshop on Non-contact Atomic Force Microscopy (Osaka, July 21–23, 1998, edited by S. Morita and M. Tsukada) Appl. Surf. Sci. **140** (1999) 243–456
[10] Proceedings of the Second International Workshop on Non-contact Atomic Force Microscopy (Pontresina, September 1–4, 1999, edited by R. Bennewitz, Ch. Gerber, and E. Meyer) Appl. Surf. Sci. **157** (2000) 207–428
[11] Proceedings of the Third International Conference on Non-contact Atomic Force Microscopy (Hamburg, July 16–19, 2000, edited by U. D. Schwarz, H. Hölscher, and R. Wiesendanger) Appl. Phys. A **72** (2001) S1-S141
[12] T. R. Albrecht, P. Grütter, D. Horne, and D. Rugar, J. Appl. Phys. **69** (1991) 668
[13] F. J. Giessibl, H. Bielefeldt, S. Hembacher, and J. Mannhart, Appl. Surf. Sci. **140** (1999) 352
[14] R. Perez, I. Stich, M. C. Payne, and K. Terakura, Phys. Rev. Lett. **78** (1997) 678
[15] R. Perez, I. Stich, M. C. Payne, and K. Terakura, Phys. Rev. B **58** (1998) 10835
[16] K. D. Brommer, B. E. Larson, M. Needels, and J. D. Joannopoulos, Jpn. J. Appl. Phys. **32** (1993) 1360
[17] F. J. Giessibl, S. Hembacher, H. Bielefeldt, and J. Mannhart, Science **289** (2000) 422
[18] ThermoMicroscopes Inc., 1171 Borregas Ave., Sunnyvale, CA 94089, USA
[19] F. J. Giessibl and B. M. Trafas, Rev. Sci. Instrum. **65** (1994) 1923

[20] F. J. Giessibl, Appl. Phys. Lett. **76** (2000) 1470
[21] F. J. Giessibl, Habilitation thesis, Augsburg University 2000
[22] Nanosurf AG, 4410 Liestal, Switzerland
[23] R. Lüthi, E. Meyer, M. Bammerlin, A. Baratoff, T. Lehmann, L. Howald, Ch. Gerber, and H.-J. Güntherodt, Z. Phys. B **100** (1996) 165
[24] F. J. Giessibl, Phys. Rev. B **56** (1997) 16010
[25] F. J. Giessibl, Appl. Phys. Lett. **78** (2001) 123
[26] F. J. Giessibl and H. Bielefeldt, Phys. Rev. B **61** (2000) 9968
[27] U. Dürig, New Journal of Physics **2** (2000) 5.1
[28] M. Z. Bazant, E. Kaxiras, and J. F. Justo, Phys. Rev. B **56** (1997) 8542
[29] H. C. Hamaker, Physica **4** (1937) 1058
[30] J. Israelachvili, Intermolecular and Surface Forces, 2nd ed., Academic Press, London 1991
[31] T. J. Senden and C. J. Drummond, Colloids Surf. A **94** (1995) 29
[32] H. Hölscher, U. D. Schwarz, and R. Wiesendanger, Appl. Surf. Sci. **140** (1999) 344
[33] F. H. Stillinger and T. A. Weber, Phys. Rev. B **31** (1985) 5262
[34] F. F. Abraham, I. P. Batra, and S. Ciraci, Phys. Rev. Lett. **60** (1988) 1314
[35] M. A. Lantz, H. J. Hug, P. J. A. van Schendel, R. Hoffmann, S. Martin, A. Baratoff, A. Abdurixit, H.-J. Güntherodt, and Ch. Gerber, Phys. Rev. Lett. **84** (2000) 2642
[36] M. A. Lantz, H. J. Hug, R. Hoffmann, P. J. A. van Schendel, P. Kappenberger, S. Martin, A. Baratoff, and H.-J. Güntherodt, Science **291** (2001) 2580
[37] C. Laschinger, diploma thesis, Augsburg University 2001
[38] L. Olsson, N. Lin, V. Yakimov, and R. Erlandsson, J. Appl. Phys. **84** (1998) 668
[39] R. P. Feynman, R. B. Leighton, and M. Sands, The Feynman Lectures on Physics , Vol. II, chapters 6–7, Sixth Printing, Addison Wesley, Reading 1977
[40] R. McWeeny, Coulson's Valence, p. 42, Oxford University Press, Oxford 1991
[41] J. E. Demuth, U. Köhler, and R. J. Hamers, J. Microsc. **151** (1988) 299
[42] C. J. Chen, J. Vac. Sci. Technol. A **1** (1991) 44
[43] C. J. Chen, Introduction to Scanning Tunneling Microscopy, p. 88, Oxford University Press 1993
[44] H. J. Hug, M. A. Lantz, A. Abdurixit, P. J. A. van Schendel, R. Hoffmann, P. Kappenberger, and A. Baratoff, Science **291** (2001) 2509a, online available at www.sciencemag.org/ cgi/ content/ full/291/5513/2509a.
[45] F. J. Giessibl, S. Hembacher, H. Bielefeldt, and J. Mannhart, Science **291** (2001) 2509a, online available at www.sciencemag.org/ cgi/ content/ full/291/5513/2509a.
[46] S. H. Ke, T. Uda, and K. Terakura, Phys. Rev. B **59** (1999) 13267
[47] U. D. Schwarz, H. Hölscher, and R. Wiesendanger, Phys. Rev. B **62** (2000) 13089
[48] H. Hölscher, W. Allers, U. D. Schwarz, A. Schwarz, and R. Wiesendanger, Appl. Phys. A **72** (2001) S35
[49] M. Guggisberg, M. Bammerlin, A. Baratoff, R. Lüthi, Ch. Loppacher, F. M. Battiston, J. Lü, R. Bennewitz, E. Meyer, and H.-J. Güntherodt, Surf. Sci. **461** (2000) 255
[50] F. J. Giessibl, S. Hembacher, H. Bielefeldt, and J. Mannhart, Appl. Phys. A **72** (2001) S15
[51] S. Y. Tong, H. Huang, C. M. Wei, W. E. Packard, F. K. Men, G. Glander, M. B. Webb, J. Vac. Sci. Technol. A **6** (1988) 615
[52] N. Ashcroft and N. D. Mermin, Solid State Physics, Saunders College, Philadelphia 1981
[53] R. Lüthi, E. Meyer, M. Bammerlin, A. Baratoff, L. Howald, Ch. Gerber, and H.-J. Güntherodt, Surface Review and Letters **4** (1997) 1025
[54] M. Bammerlin, R. Lüthi, E. Meyer, A. Baratoff, J. Lü, M. Guggisberg, Ch. Gerber, L. Howald, and H.-J. Güntherodt, Probe Microscopy **1** (1997) 3
[55] H. Ueyama, Y. Sugawara, and S. Morita, Appl. Phys. A **66** (1998) S295
[56] U. Dürig, Surf. Interface Anal. **27** (1999) 467
[57] M. Gauthier and M. Tsukada, Phys. Rev. Lett. **84** (1999) 2642; Phys. Rev. B **60** (1999) 11716
[58] A. Abdurixit, A. Baratoff, and E. Meyer, Appl. Surf. Sci. **157** (2000) 355
[59] N. Sasaki and M. Tsukada, Jpn. J. Appl. Phys. **39** Part 2 (2000) L1334